

# Chapter 1

## Tests of Theory in Rydberg States of One-electron Ions

Joseph N. Tan and Peter J. Mohr

Comparison of optical frequency measurements to predictions of quantum electrodynamics (QED) for Rydberg states of one-electron ions can test theory and allow new determinations of constants of nature to be made. Simplifications in the QED theory of high-angular-momentum states reduces the uncertainty in the prediction of transition frequencies to a level where a new value of the Rydberg constant which is independent of the proton radius can be determined. Since the energy-level spacing between neighboring Rydberg states grows as the square of the nuclear charge number, it is possible to study transitions with optical frequencies that are accessible to femtosecond laser frequency combs. Recently at the US National Institute of Standards and Technology (NIST), highly-charged ions (including bare nuclei) created in an Electron Beam Ion Trap (EBIT) were extracted and captured in a novel compact Penning trap. An ongoing experiment aims to produce one-electron ions isolated in an ion trap designed for laser spectroscopy. Tests of theory in a regime free of nuclear effects would be valuable in shedding light on the puzzle surrounding the large discrepancy in the value of the proton radius inferred from the observed Lamb shift in muonic hydrogen as compared to the value deduced from hydrogen and deuterium spectroscopy and electron scattering measurements.

### 1.1 Introduction

Quantum electrodynamics (QED) is the first satisfactory quantum description of the interaction of charged particles (and antiparticles) via the exchange of photons and

---

Joseph N. Tan  
National Institute of Standards and Technology, 100 Bureau Drive, Gaithersburg, MD 20899,  
U.S.A. e-mail: joseph.tan@nist.gov

Peter J. Mohr  
National Institute of Standards and Technology, 100 Bureau Drive, Gaithersburg, Maryland 20899,  
U.S.A. e-mail: mohr@nist.gov

of the creation and annihilation of elementary particles. QED makes precise predictions for various physical quantities, and these predictions have been tested across a vast array of phenomena. Spectroscopic measurements in atoms have played a crucial role in spurring the development of QED to be the most accurate physical theory yet invented.

This success seems all the more remarkable because, as the quantum field theory of electrons and photons, QED does not remove the divergences well known in Maxwell's classical theory of electromagnetism; on the contrary, new infinities are found in QED, associated with virtual processes in the vacuum. Sensible, finite results are obtainable only after renormalization; this is an art inextricably tied to the introduction of fundamental constants, such as the electron mass and charge, into the theory.

One-electron atomic systems are among the simplest quantum-mechanical objects that have enabled very stringent tests of QED to be made, yielding some of the most precise measurements of fundamental constants. For example, the value of the Rydberg constant recommended by the Committee on Data for Science and Technology (CODATA), an interdisciplinary scientific committee of the International Council for Science (ICSU), is obtained from precise measurements of various transitions in hydrogen and its stable isotope deuterium taken together with electron scattering measurements [1].

For over a hundred years, the study of hydrogen-like atoms has contributed to our understanding of the quantum world. Figure 1.1 illustrates the eight orders-of-magnitude improvement in the accuracy of the Rydberg constant in a 130-year history that includes many theoretical and experimental discoveries and developments [2, 3]. As another example, assuming the validity of quantum electrodynamics (QED) calculations at the tenth order, the fine-structure constant  $\alpha$  (the universal constant of electromagnetic interactions) is most precisely obtained from the electron  $|g| - 2$  experiment, which measures the anomalous magnetic moment of a single electron stored in a Penning trap (dubbed *geonium*, an engineered atom consisting of one electron bound to the earth).

The first tests of the emerging formalism of QED came shortly after World War II. Ref. [4] reported the first measurement of the anomalous magnetic moment of the electron; in the same year, Ref. [5] presented the first measurement of the "Lamb shift" of the  $2s$  level of hydrogen [6], another departure from the Dirac theory of the hydrogen atom. These discoveries have led to more stringent tests of QED, with remarkable progress over six decades. On the one hand, with control and minimization of cavity effects that limited early *geonium*  $|g| - 2$  experiments [7, 8], the magnetic moment of the electron  $|g| = 2(1 + a_e)$  has been measured recently at Harvard University with a relative uncertainty of  $2.8 \times 10^{-13}$  using a single electron isolated in a cylindrical Penning trap [9]; by comparison, the calculated magnetic moment of the electron has a relative uncertainty of  $5.2 \times 10^{-12}$  coming mainly from the uncertainty of the best independent determination of the fine-structure constant. On the other hand, the hydrogen  $1s - 2s$  transition has been measured with a relative uncertainty of  $1.4 \times 10^{-14}$  [10]; here a test of theory is hampered by uncertainties in the nuclear-size corrections.

Currently the accuracy in the determination of the Rydberg constant has a relative uncertainty of  $5.0 \times 10^{-12}$  [1]. It seems astonishing that QED should have attained such high accuracy based on abstractions employed to represent physical objects and measurements, particularly when one of the pioneers in its development has noted the “mathematical inconsistencies and renormalized infinities swept under the rug” [11].

Looking to the future, in Section 1.5, we consider possible determinations of fundamental constants and tests of theory in Rydberg states of one-electron ions. This has been discussed in [12], where it was pointed out that the problems that limit the theoretical predictions in low-angular-momentum states are strongly suppressed in Rydberg states with high angular momentum (high- $l$ ), because the electron has a very small probability of being near the nucleus in such states. Remarkably, the simplification of higher-order QED terms in Rydberg states yields an overall theoretical uncertainty that is smaller than the uncertainties propagated from the fundamental constants. In particular, even with its currently-assigned uncertainty of  $5.0 \times 10^{-12}$ , the Rydberg constant is the leading source of uncertainty in this regime, larger than the uncertainties due to other constants by a factor of 100. Hence, if precise measurements can be made for comparison with theory, one-electron ions in Rydberg states can be useful in testing QED in a regime with negligible nuclear effects. Assuming that QED remains valid, this could enable a Rydberg constant determination

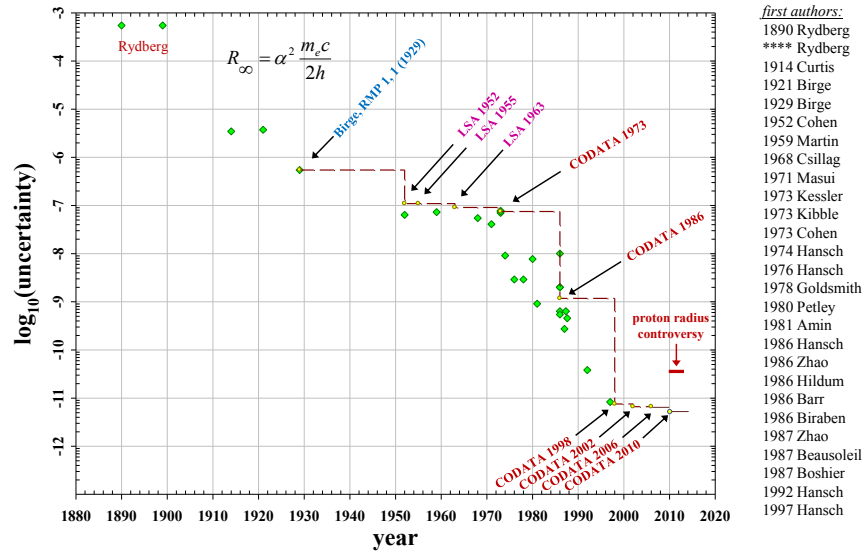


**Fig. 1.1** Relative uncertainty in the determinations of the Rydberg constant over its history. Diamonds stand for uncertainties in experimental values; circles with dashed lines stand for uncertainties in least-squares adjustments (LSA). Its current uncertainty of  $5 \times 10^{-12}$  does not take into account the puzzling  $7 \sigma$  discrepancy in the proton radius described in Sec. 1.3.

that is independent of the proton radius. As discussed in section 1.3, interest in such a determination is heightened by the large discrepancy in the proton radius determined from the recent measurement of the muonic hydrogen Lamb shift compared to the determinations of the radius by other methods, which potentially would be impacted by an independent measurement of the Rydberg constant. In section 1.6, we describe an experimental effort at NIST to make one-electron ions in Rydberg states via charge transfer from highly-excited atom to bare nuclei isolated in a trap.

## 1.2 The Rydberg Constant

The Rydberg constant is a combination of fundamental constants:

$$R_\infty = \alpha^2 m_e c / 2h, \quad (1.1)$$

where  $h$  is the Planck constant,  $c$  is the speed of light,  $m_e$  is the electron mass, and  $\alpha$  is the fine-structure constant. It plays a pivotal role in the CODATA least-square adjustments. Historically, it first appeared as the overall coefficient in the mathematical formula connecting the light frequency (or wavelength) to the numbers characterizing the atomic states involved in the light emission. This relationship was first discovered phenomenologically in the spectral line emissions of hydrogen by Johann Balmer, who showed that the visible lines in the series named after him are related by a simple formula involving integers. Inspired by this discovery, Johannes Rydberg showed that a more general formula which included small non-integral offsets (now called “quantum defects”) has much broader application by accounting for perturbations due to core electrons when studying atoms with one highly-excited electron (Rydberg atoms) [13]. Figure 1.1 shows the improvement in the determinations of the Rydberg constant going back over one hundred years; a compilation of the experimental values can be found in Ref. [3].

The CODATA recommended value of the Rydberg constant has been obtained primarily by comparing theory and experiment for twenty-four transition frequencies or pairs of frequencies in hydrogen and deuterium [1]. The theoretical value for each transition is the product of the Rydberg constant and a calculated factor based on QED that also depends on other constants. While the most accurately measured transition frequency in hydrogen (1S–2S) has a relative uncertainty of  $1.4 \times 10^{-14}$  [10], the recommended value of the Rydberg constant has a larger relative uncertainty of  $5.0 \times 10^{-12}$  which is essentially the uncertainty in the theoretical factor which includes the proton radius. The main source of uncertainty in the theoretical factor is from the charge radius of the proton with additional uncertainty due to uncalculated or partially calculated higher-order terms in the QED corrections.

### 1.3 The Proton Radius Puzzle: Is QED in trouble?

The uncertainty introduced into the theory of hydrogen and deuterium transition frequencies due to uncertainty in the proton and deuteron charge radii can be reduced by employing accurate independent determinations of the radii. Electron-proton and electron-deuteron scattering experiments are important sources of information about the radii. Potentially more accurate information is provided by comparison of theory and experiment for muonic hydrogen. In this section, the various sources of information on the charge radii are briefly reviewed, and the discrepancy that leads to the proton radius puzzle is described.

#### 1.3.1 Spectroscopic data and the Rydberg constant

Values of the Rydberg constant and the proton and deuteron charge radii follow from precise spectroscopic measurements on hydrogen and deuterium. For the 2010 CODATA determination of the constants, 24 frequencies or differences of frequencies were taken into account. These data are listed in Table 1.1. Comparison of theory and experiment, which does not include electron scattering values for the radii, leads to a value of the Rydberg constant given by [1]

$$R_{\infty} = 10973731.568521(82) \text{ m}^{-1}, \quad (1.2)$$

which has a relative uncertainty of  $7.4 \times 10^{-12}$ , and a value for the proton radius given by [1]

$$r_p = 0.8758(77) \text{ fm}. \quad (1.3)$$

The theoretical input used in the analysis is described in [1]. The main source of uncertainty, as has been mentioned, is the uncertainty in the proton charge radius. A smaller, but not negligible, uncertainty arises from uncalculated theoretical contributions.

#### 1.3.2 Scattering determinations of the radii

The accuracy of the Rydberg constant extracted from hydrogen and deuterium spectroscopic data can be improved by including information on the nuclear charge radii from electron scattering experiments in the analysis. Electron-proton scattering data values of the proton radius  $r_p$  and an electron-deuteron scattering data value of the deuteron radius  $r_d$  used as input data in the 2010 CODATA adjustment are

$$r_p = 0.895(18) \text{ fm}, \quad (1.4)$$

**Table 1.1** Measured frequencies  $\nu$  considered in the LSA determination of the Rydberg constant  $R_\infty$  (H is hydrogen and D is deuterium).

	Frequency interval(s)	Reported value $\nu/\text{kHz}$	Rel. stand. uncert. $u_r$
	MPQ 2004 (Fischer <i>et al.</i> [14])		
1	$\nu_H(1S_{1/2} - 2S_{1/2})$	2466061413187.080(34)	$1.4 \times 10^{-14}$
	MPQ 1995 (Weitz <i>et al.</i> [15])		
2	$\nu_H(2S_{1/2} - 4S_{1/2}) - \frac{1}{4}\nu_H(1S_{1/2} - 2S_{1/2})$	4797338(10)	$2.1 \times 10^{-6}$
3	$\nu_H(2S_{1/2} - 4D_{5/2}) - \frac{1}{4}\nu_H(1S_{1/2} - 2S_{1/2})$	6490144(24)	$3.7 \times 10^{-6}$
4	$\nu_D(2S_{1/2} - 4S_{1/2}) - \frac{1}{4}\nu_D(1S_{1/2} - 2S_{1/2})$	4801693(20)	$4.2 \times 10^{-6}$
5	$\nu_D(2S_{1/2} - 4D_{5/2}) - \frac{1}{4}\nu_D(1S_{1/2} - 2S_{1/2})$	6494841(41)	$6.3 \times 10^{-6}$
	MPQ 2010 (Parthey <i>et al.</i> [16])		
6	$\nu_D(1S_{1/2} - 2S_{1/2}) - \nu_H(1S_{1/2} - 2S_{1/2})$	670994334.606(15)	$2.2 \times 10^{-11}$
	LKB/SYRTE 1997 (de Beauvoir <i>et al.</i> [16])		
7	$\nu_H(2S_{1/2} - 8S_{1/2})$	770649350012.0(8.6)	$1.1 \times 10^{-11}$
8	$\nu_H(2S_{1/2} - 8D_{3/2})$	770649504450.0(8.3)	$1.1 \times 10^{-11}$
9	$\nu_H(2S_{1/2} - 8D_{5/2})$	770649561584.2(6.4)	$8.3 \times 10^{-12}$
10	$\nu_D(2S_{1/2} - 8S_{1/2})$	770859041245.7(6.9)	$8.9 \times 10^{-12}$
11	$\nu_D(2S_{1/2} - 8D_{3/2})$	770859195701.8(6.3)	$8.2 \times 10^{-12}$
12	$\nu_D(2S_{1/2} - 8D_{5/2})$	770859252849.5(5.9)	$7.7 \times 10^{-12}$
	LKB/SYRTE 1999 (Schwob <i>et al.</i> [17])		
13	$\nu_H(2S_{1/2} - 12D_{3/2})$	799191710472.7(9.4)	$1.2 \times 10^{-11}$
14	$\nu_H(2S_{1/2} - 12D_{5/2})$	799191727403.7(7.0)	$8.7 \times 10^{-12}$
15	$\nu_D(2S_{1/2} - 12D_{3/2})$	799409168038.0(8.6)	$1.1 \times 10^{-11}$
16	$\nu_D(2S_{1/2} - 12D_{5/2})$	799409184966.8(6.8)	$8.5 \times 10^{-12}$
	LKB 2010 (Arnoult <i>et al.</i> [18])		
17	$\nu_H(1S_{1/2} - 3S_{1/2})$	2922743278678(13)	$4.4 \times 10^{-12}$
	LKB 1996 (Bourzeix <i>et al.</i> [19])		
18	$\nu_H(2S_{1/2} - 6S_{1/2}) - \frac{1}{4}\nu_H(1S_{1/2} - 3S_{1/2})$	4197604(21)	$4.9 \times 10^{-6}$
19	$\nu_H(2S_{1/2} - 6D_{5/2}) - \frac{1}{4}\nu_H(1S_{1/2} - 3S_{1/2})$	4699099(10)	$2.2 \times 10^{-6}$
	Yale 1995 (Berkeland <i>et al.</i> [20])		
20	$\nu_H(2S_{1/2} - 4P_{1/2}) - \frac{1}{4}\nu_H(1S_{1/2} - 2S_{1/2})$	4664269(15)	$3.2 \times 10^{-6}$
21	$\nu_H(2S_{1/2} - 4P_{3/2}) - \frac{1}{4}\nu_H(1S_{1/2} - 2S_{1/2})$	6035373(10)	$1.7 \times 10^{-6}$
	Harvard 1994 (Hagley and Pipkin [21])		
22	$\nu_H(2S_{1/2} - 2P_{3/2})$	9911200(12)	$1.2 \times 10^{-6}$
	Harvard 1986 (Lundeen and Pipkin [22])		
23	$\nu_H(2P_{1/2} - 2S_{1/2})$	1057845.0(9.0)	$8.5 \times 10^{-6}$
	U. Sussex 1979 (Newton <i>et al.</i> [23])		
24	$\nu_H(2P_{1/2} - 2S_{1/2})$	1057862(20)	$1.9 \times 10^{-5}$

<sup>1</sup> MPQ: Max-Planck-Institut für Quantenoptik, Garching. LKB: Laboratoire Kastler-Brossel, Paris. SYRTE: Systèmes de référence Temps Espace, Paris, formerly Laboratoire Primaire du Temps et des Fréquences (LPTF).

$$r_p = 0.8791(79) \text{ fm}, \quad (1.5)$$

$$r_d = 2.130(10) \text{ fm}. \quad (1.6)$$

The value of  $r_p$  in Eq. (1.4) is based on Sick's analysis of the world data available at the time [24]. Equation (1.5) gives a value based on measurements made at the Mainz Microtron MAMI and analyzed using a variety of form-factor models [25]. The result for  $r_d$  in Eq. (1.6) is the result of an analysis of the world data by Sick [26].

More recent values for the proton radius from scattering data have been given since the 2010 CODATA cutoff date for input data. Precise measurement of the ratio of the electric to magnetic form factors over a range of  $Q^2$  was made at the Thomas Jefferson National Accelerator facility in Virginia (JLab). These data, combined with selected earlier data, yield the value  $r_p = 0.875(10) \text{ fm}$  [27, 28]. Sick has obtained  $r_p = 0.894(8) \text{ fm}$  [29] and  $r_p = 0.886(8) \text{ fm}$  [30] by supplementing the scattering data with a calculation of the shape of the large radius proton charge distribution. The analysis leading to the latter value for  $r_p$  includes data from Ref. [25]. An analysis of existing data with an analytic form-factor model has yielded a smaller radius  $r_p = 0.8489(69) \text{ fm}$  [31].

The consensus of these values is consistent with the 2010 CODATA recommended value for the proton radius. Exceptions are the result of [29] which is slightly larger and the result of [31] which is significantly smaller. The various treatments of the electron scattering data and the difficulties in arriving at a unique result for the proton radius are discussed in Ref. [32].

### 1.3.3 Proton radius from muonic hydrogen

It is expected that a better value for the proton radius, which would lead to a better value for the Rydberg constant, can be obtained from muonic hydrogen, an atom consisting of a negative muon and a proton. Due to its larger mass, the Bohr radius of the muon is about 207 times smaller than the electron Bohr radius. As a result, the splitting of the 2S and 2P states in muonic hydrogen is quite sensitive to the size of the proton, which contributes about 2% to the total Lamb shift. (Because of the large electron-vacuum-polarization effect, the  $2S_{1/2}$  level is below both the  $2P_{3/2}$  and  $2P_{1/2}$  levels.)

In measurements carried out at the Paul Scherrer Institute (PSI), Villigen, Switzerland, the  $2S_{1/2}(F=1) - 2P_{3/2}(F=2)$  and  $2S_{1/2}(F=0) - 2P_{3/2}(F=1)$  transitions in muonic hydrogen have been accurately measured [33, 34, 35]. These results, when combined with the theory for the transition, lead to [35]

$$r_p = 0.84087(39) \text{ fm}. \quad (1.7)$$

Because of the discrepancy between this value of the proton radius and the values obtained from spectroscopic data or electron scattering data, the theory for the

transition frequency has been reviewed many times. Recent reviews, which also list earlier reviews, are given in Refs. [32, 36, 37, 38, 39, 40, 41, 42].

### 1.3.4 Comparison of the determinations of the proton radius

Values of the proton radius discussed in Secs. 1.3.1-1.3.3 are shown in Fig. 1.2. Based on both spectroscopic data and the electron scattering data, the CODATA recommended value of the Rydberg constant is [1]

$$R_\infty = 10973731.568539(55) \text{ m}^{-1} \quad (1.8)$$

which has a relative uncertainty of  $5.0 \times 10^{-12}$ , and the recommended value of the proton radius is [1]

$$r_p = 0.8775(51) \text{ fm}. \quad (1.9)$$

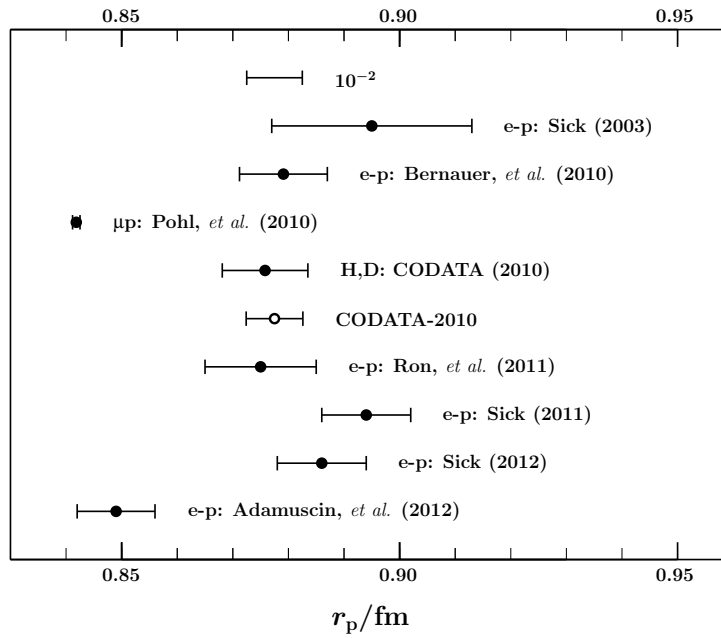


**Fig. 1.2** Values of the proton radius  $r_p$  given in Secs. 1.3.1-1.3.3. The entry at the top sets the scale for the graph. The values, from top to bottom, are from Refs. [24, 43], [25], [33, 35], [1], [1], [27, 28], [29], [30], [31]. Error bars represent 1 standard uncertainty.

If the proton radius from muonic hydrogen in Eq. (1.7) is compared to the CODATA 2010 recommended value in Eq. (1.9), there is a  $7\sigma$  disagreement. If it is compared to the value in Eq. (1.3), based on only H and D spectroscopic data, the disagreement is  $4.5\sigma$ .

Alternatively, if the proton radius derived from muonic hydrogen is included among the input data for a least-squares adjustment of the spectroscopic data, the result is an apparent inconsistency between the fitted values of the transition frequencies and the experimental values used as the input data, as shown in Fig. 1.3 [1]. An additional problem with including the muonic hydrogen proton radius in a least-squares analysis of the spectroscopic data is that it leads to a value of the fine-structure constant given by  $\alpha^{-1} = 137.035881(35) [2.6 \times 10^{-7}]$ , which differs from the 2010 recommended value by  $3.4\sigma$  [1]. The value of  $R_\infty$  from such an adjustment is [1]

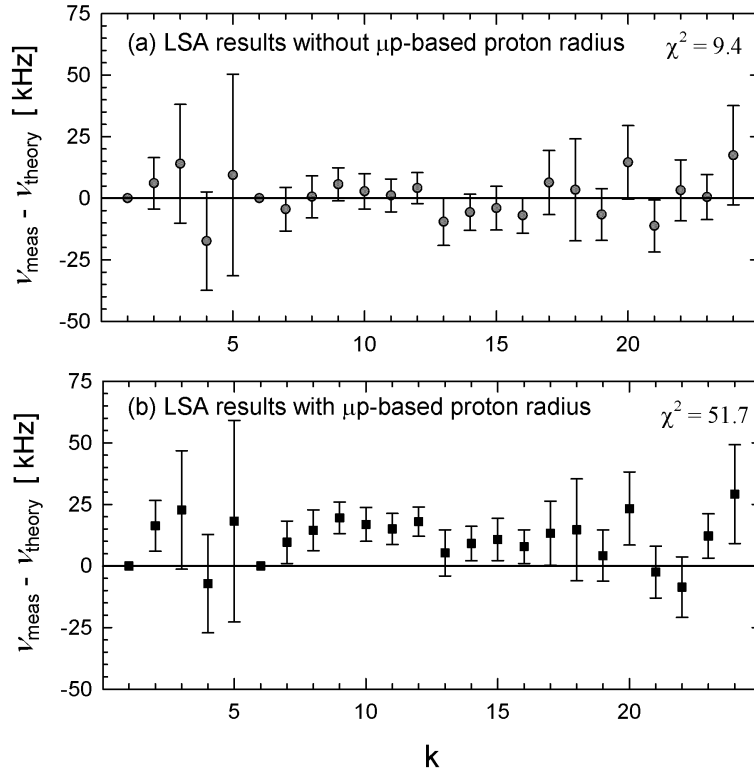


**Fig. 1.3** Transition frequencies in hydrogen and deuterium. Deviations from theory are large when the proton radius deduced from the muonic hydrogen Lamb-shift is included among the input data. Error bars represent 1 standard uncertainty.

$$R_\infty = 10\,973\,731.568\,175(12)\,\text{m}^{-1}. \quad (1.10)$$

This value of the Rydberg constant differs from the 2010 recommended value by  $6.5\sigma$ .

These discrepancies constitute the proton radius puzzle. At this time, there is no explanation for the disagreements between the muonic hydrogen Lamb shift data and both the H and D spectroscopic data and the electron-proton scattering data. It may be necessary to modify QED to properly account for the muon data, or there still may be a contribution from conventional QED that has not been taken into account properly.

### *1.3.5 Comparison of the determinations of the Rydberg constant*

As shown in the previous sections, there is disagreement between the values of the Rydberg constant determined from the H and D spectroscopic data with and without the inclusion of the proton radius data from muonic hydrogen. The reason for this is that S states play an important role in the determination of the Rydberg constant in the least-squares adjustments, and these states are relatively strongly affected by the size of the nucleus.

On the other hand, there is the possibility of using Rydberg states to determine the Rydberg constant. Such a determination would be virtually independent of the proton or nuclear radius, because high- $\ell$  states have a negligible overlap with the nucleus. Thus such an independent value for the Rydberg constant might favor one of the values associated with either including or not including the muonic hydrogen proton radius in the analysis, thereby shedding light on the proton radius puzzle.

In this regard, it is of interest to note that there is an existing unpublished measurement of the Rydberg constant made in Rydberg states [44]

$$R_\infty = 10\,973\,731.56834(23)\,\text{m}^{-1} \quad (1.11)$$

Values for the Rydberg constant in Eqs. (1.8), (1.10), and (1.11) are shown in Fig. 1.4. It is apparent from that figure that an independent determination of the Rydberg constant from Rydberg states with even a modest accuracy might distinguish between the values involving S states with or without the muonic hydrogen data included.

## **1.4 Optical transitions between Rydberg states**

Optical frequency combs [45] can be used to make precise measurements of optical transitions between Rydberg states. For example, laser spectroscopy of antiprotonic helium together with theoretical calculations of the atomic structure have been used

to weigh the antiproton [46]. On the other hand, if *CPT* symmetry is assumed, the experiments and theory can be interpreted as a determination of the electron mass.

For one-electron ions in Rydberg states, the optical frequency combs have the potential of making precise absolute frequency measurements which can lead to a determination of the Rydberg constant. Although transitions between Rydberg states in neutral atoms are typically in the microwave frequency range, in highly-ionized ions, the frequencies can be in the optical range, as shown in Figure 1.5. In that figure, the frequencies corresponding to transitions between adjacent Bohr energy levels ( $n$  to  $n - 1$ ) in hydrogen-like ions are shown as a function of the principle quantum number of the upper level  $n$  and the charge number of the nucleus  $Z$ . The colored bands indicate the (optical) colors corresponding to the frequencies in that figure. The pink band is approximately the region of infra-red frequencies.

Much of this parameter space is accessible to optical frequency synthesizers based on mode-locked femtosecond lasers, which readily provide ultra-precise reference rulers (optical frequency combs) spanning the near-infrared and visible region of the optical spectrum (530 nm–2100 nm). Even when the absolute accuracy is limited by the primary frequency standard (a few parts in  $10^{16}$ ), optical frequency

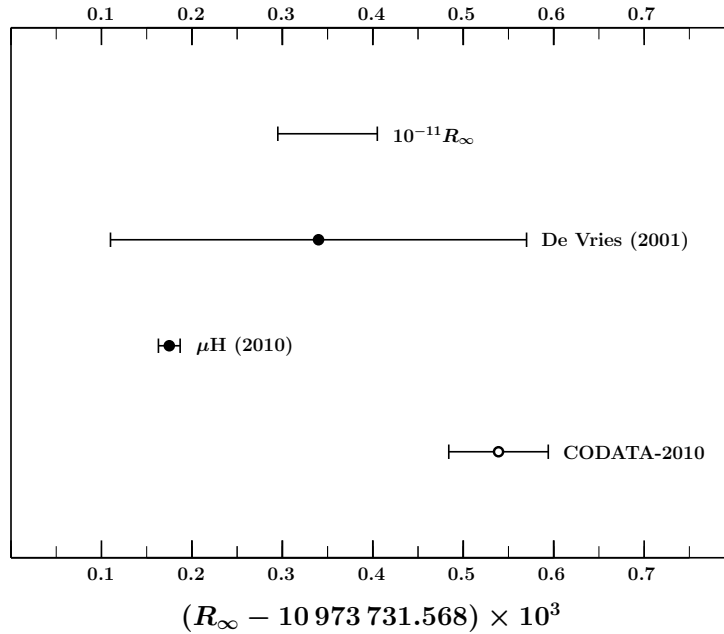


**Fig. 1.4** Values of the Rydberg constant based on microwave transitions in circular states of hydrogen, the value obtained by including the muonic hydrogen proton radius in the least-squares adjustment of H and D data, and the 2010 recommended value. First entry sets the scale of the graph. Error bars represent 1 standard uncertainty.

combs can enable relative frequency measurements with uncertainties approaching 1 part in  $10^{19}$  over 100 THz of bandwidth [47]—making comb-based measurements generally more precise than other existing technologies. The precisely controlled pulse train from a femtosecond laser can also be used directly to probe the global atomic structure, thus integrating the optical, tera-Hertz, and radio-frequency domains [48].

This is an advantage, because heavier hydrogen-like ions with a higher nuclear charge  $Z$  have larger fine-structure separations, which scale as  $Z^4$ . As a consequence, the Rydberg states are far more robust against perturbations such as Stark mixing than Rydberg states in the microwave regime. In addition, the charged ions repel each other, so the effect of short range collisions can be expected to be less important.

### 1.5 Theory of Rydberg states

In this section, we consider the theory of one-electron ions in Rydberg states, focusing on aspects unique to the high- $\ell$  case. In particular, simplifications in the theory reduce the uncertainties and allow accurate predictions of the energy levels to be made. Radiative transitions are also discussed.

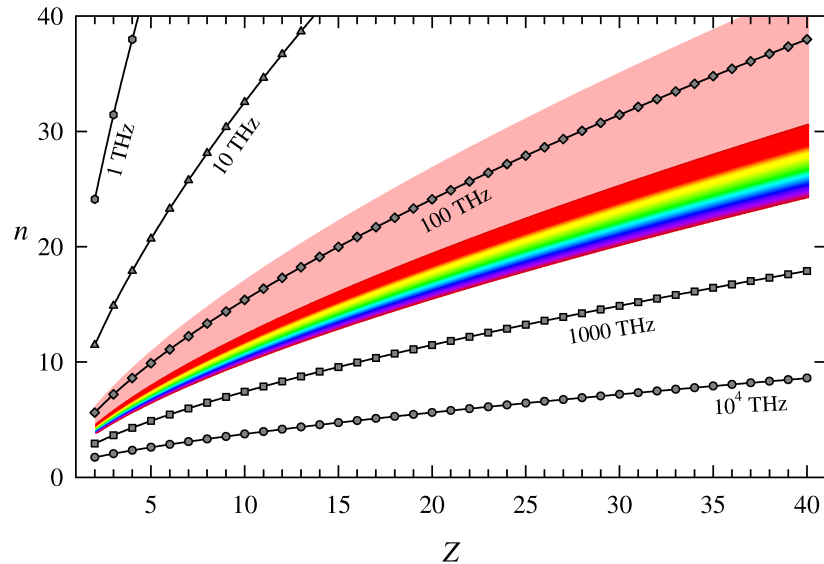


**Fig. 1.5** Iso-frequency plots showing values of  $Z$  and approximate  $n$  that give a specified value of the frequency for transitions changing the principal quantum number  $n$  by 1 in a one-electron ion with nuclear charge  $Z$ . Color bands represent frequencies in the near infrared and visible region.

### 1.5.1 Simplification of nuclear size and higher-order QED effects

The largest source of uncertainty in determining the Rydberg constant from spectroscopy of H and D is the uncertainty in the nuclear radius, which translates into uncertainty in the theoretical values of the transition frequencies. For states with high orbital angular momenta  $\ell$ , this uncertainty is relatively smaller than in lower- $\ell$  states, because in the high- $\ell$  case, the probability  $P(r)$  for the electron to be found within a short distance  $r$  of the nucleus is very low. As a consequence, the nuclear-size correction to the energy level is small, and knowledge of the nuclear size is unimportant. For a Rydberg state of a hydrogen-like ion with charge number  $Z$ , high principal quantum number  $n$ , and angular momentum  $\ell = n - 1$ , this probability is

$$P(r) = \int_{|\mathbf{x}| < r} d\mathbf{x} |\psi(\mathbf{x})|^2 \approx \frac{1}{(2n+1)!} \left( \frac{2Zr}{na_0} \right)^{2n+1}, \quad (1.12)$$

where  $a_0$  is the Bohr radius. If  $r$  is taken to be the nuclear radius, then the high-power factor, together with the factorial in the denominator, leads to an almost complete suppression of nuclear effects for circular or near-circular Rydberg states. For example, if  $n = 5$  and  $Z = 5$ , then  $P(1 \text{ fm}) \approx 10^{-56}$ .

Another advantage of high- $\ell$  states for theory is the fact that the higher-order corrections in the QED theory of the levels are relatively smaller for these states compared to low- $\ell$  states. Thus, the perturbation expansion of the theoretical expressions for the energy levels, as a function of  $Z\alpha$ , provides relatively more accurate results with a given number of terms.

Since these two portions of the theory have the largest associated uncertainties, their elimination significantly reduces the relative uncertainty for the theory of the transition frequencies to the extent that in certain cases the Rydberg constant is the largest source of uncertainty. Then, a comparison of theory and experiment for the transitions can provide information on the Rydberg constant and potentially improve its accuracy.

### 1.5.2 High- $\ell$ -state energy levels in hydrogen-like atoms

In this section, we list the known theoretical expressions for the energy levels of hydrogen-like ions and give numerical results with estimates of the uncertainties for special cases. Reviews of the theory and references to original work are given in [49, 50, 1]. Here the theory is given only for  $\ell \geq 2$ .

The energy levels can be written as

$$E_n = E_{\text{DM}} + E_{\text{RR}} + E_{\text{QED}}, \quad (1.13)$$

a sum of the Dirac energy with nuclear motion corrections  $E_{\text{DM}}$ , relativistic recoil corrections  $E_{\text{RR}}$ , and radiative corrections  $E_{\text{QED}}$ .

For the first term, the difference between the Dirac eigenvalue  $E_D$  and the electron rest energy, is proportional to

$$\alpha^2 D m_e c^2 = E_D - m_e c^2 = \left( \left[ 1 + \frac{(Z\alpha)^2}{(n-\delta)^2} \right]^{-1/2} - 1 \right) m_e c^2, \quad (1.14)$$

$$\alpha^2 D = -\frac{(Z\alpha)^2}{2n^2} + \left( \frac{3}{8n} - \frac{1}{2j+1} \right) \frac{(Z\alpha)^4}{n^3} + \dots, \quad (1.15)$$

where  $j$  is the total angular momentum quantum number,  $\delta = |\kappa| - \sqrt{\kappa^2 - (Z\alpha)^2}$ , and  $\kappa = (-1)^{\ell+j+1/2}(j+1/2)$  is the Dirac spin-angular quantum number. The expansion in Eq. (1.15) shows the leading Schrödinger and fine-structure terms. The energy level, taking into account the leading nuclear motion effects, is given by [50]

$$E_{DM} = 2hcR_\infty \left[ \mu_r D - \frac{r_N \mu_r^3 \alpha^2}{2} D^2 + \frac{r_N^2 \mu_r^3 Z^4 \alpha^2}{2n^3 \kappa (2\ell+1)} \right], \quad (1.16)$$

where  $r_N = m_e/m_N$  is the ratio of the electron mass to the nucleus mass, and  $\mu_r = 1/(1+r_N)$  is the ratio of the reduced mass to the electron mass.

Relativistic corrections to Eq. (1.16), associated with motion of the nucleus are

$$E_{RR} = 2hcR_\infty \frac{r_N Z^5 \alpha^3}{\pi n^3} \left\{ \mu_r^3 \left[ -\frac{8}{3} \ln k_0(n, \ell) - \frac{7}{3\ell(\ell+1)(2\ell+1)} \right] \right. \\ \left. + \pi Z\alpha \left[ 3 - \frac{\ell(\ell+1)}{n^2} \right] \frac{2}{(4\ell^2-1)(2\ell+3)} + \dots \right\}, \quad (1.17)$$

where  $\ln k_0(n, \ell)$  is the Bethe logarithm. We assume that the uncertainty due to uncalculated higher-order terms is  $Z\alpha \ln(Z\alpha)^{-2}$  times the last term in Eq. (1.17).

Quantum electrodynamics (QED) corrections for high- $\ell$  states are

$$E_{QED} = 2hcR_\infty \frac{Z^4 \alpha^2}{n^3} \left\{ -\mu_r^2 \frac{a_e}{\kappa(2\ell+1)} + \mu_r^3 \frac{\alpha}{\pi} \left[ -\frac{4}{3} \ln k_0(n, \ell) \right. \right. \\ \left. \left. + \frac{32}{3} \frac{3n^2 - \ell(\ell+1)}{n^2} \times \frac{(2\ell-2)!}{(2\ell+3)!} (Z\alpha)^2 \ln \left[ \frac{1}{\mu_r (Z\alpha)^2} \right] + (Z\alpha)^2 G(Z\alpha) \right] \right\}, \quad (1.18)$$

where  $a_e$  is the electron magnetic moment anomaly and  $G(Z\alpha)$  is a function that contains higher-order QED corrections. Equation (1.19) contains no explicit vacuum polarization contribution because of the damping of the wavefunction near the origin where the polarization effect is largest. The quantity  $a_e$  replaces the order-by-order terms in the theory that are equivalent to the free-electron magnetic moment anomaly. Instead, the experimental value is used for the sum of all such terms in order to eliminate uncertainty associated with the calculated values and higher-order omitted terms. We employ the value  $a_e = 1.15965218073(28) \times 10^{-3}$  obtained in a recent experiment [51].

The dominant terms in  $G(Z\alpha)$  are expected to be of the form

$$G(Z\alpha) = A_{60} + A_{81}(Z\alpha)^2 \ln(Z\alpha)^{-2} + A_{80}(Z\alpha)^2 + \dots \\ + \frac{\alpha}{\pi} B_{60} + \dots + \left(\frac{\alpha}{\pi}\right)^2 C_{60} + \dots, \quad (1.19)$$

where the letters A, B, and C indicate contributions arising from one-, two-, and three-photon Feynman diagrams, respectively. The function  $G(Z\alpha) = G_{\text{SE}}(Z\alpha) + G_{\text{VP}}(Z\alpha)$  is the sum of contributions from self-energy (SE) diagrams and vacuum-polarization (VP) diagrams. The coefficients  $A_{60}$  and  $A_{81}$  arise from the self energy, and  $A_{80}$  arises from both the self energy and the long-range component of the vacuum polarization.

The first two terms in Eq. (1.19) come from the one-loop self energy

$$G_{\text{SE}}(Z\alpha) = A_{60} + A_{81}(Z\alpha)^2 \ln(Z\alpha)^{-2} + \dots, \quad (1.20)$$

and the leading contribution is given by the term  $A_{60}$ . Calculated values for this coefficient are given in Table 1.2 [12, 52]. Results of a complete calculation of the one-loop self energy, given in Table 1.3, are consistent with the calculation of the leading term, which provides an independent check against substantial errors in either calculation [53]. The good agreement also indicates that the higher-order terms are not significantly larger than expected. The uncertainty in  $G_{\text{SE}}(Z\alpha)$  is assumed to be given by  $A_{60}(Z\alpha)^2 \ln(Z\alpha)^{-2}$ , where the coefficient  $A_{81}$  in the first omitted term is replaced by  $A_{60}$  for the estimate.

The vacuum-polarization contribution to  $A_{80}$  is extremely small [54]. The two-photon coefficient  $B_{60}$  has not been calculated for high- $\ell$  states. However, a comparison of calculated values of  $B_{60}$  [55] and  $A_{60}$  [56] for  $\ell \leq 5$ , suggests it is of the order of  $4|A_{60}|$ , which is taken to be its uncertainty. The three-photon term  $C_{60}$  is expected to be the next term, and is assumed to be negligible.

### 1.5.3 Transition frequencies and uncertainties

To put the theory presented above into perspective, we list the numerical predictions for transition frequencies for two different ions, and indicate the various sources of uncertainties. We consider the frequency of the transition between the state with  $n = 14$ ,  $\ell = 13$ ,  $j = \frac{27}{2}$  and the state with  $n = 15$ ,  $\ell = 14$ ,  $j = \frac{29}{2}$  in the hydrogen-like ions  $\text{He}^+$  and  $\text{Ne}^{9+}$ . The constants used in the evaluation are the 2010 CODATA recommended values [1], with the exception of the neon nucleus mass  $m(^{20}\text{Ne}^{10+})$  which is taken from the neon atomic mass [57], corrected for the mass of the electrons and their binding energies. Values of the various contributions and the total are given as frequencies in Table 1.4. Standard uncertainties are listed with the numbers where they are non-negligible. The largest uncertainty arises from the Rydberg frequency  $cR_\infty$ , which is a common factor in all of the contributions. There is no un-

**Table 1.2** Calculated values for the coefficient  $A_{60}$  from [12, 52]. The numbers in parentheses are standard uncertainties in the last figure.

n	$\ell = n - 2, j = \ell - \frac{1}{2}$	$\ell = n - 1, j = \ell - \frac{1}{2}$
9	$7.018\ 373(5) \times 10^{-5}$	$3.860\ 349(5) \times 10^{-5}$
10	$3.655\ 111(5) \times 10^{-5}$	$2.158\ 923(5) \times 10^{-5}$
11	$2.008\ 438(5) \times 10^{-5}$	$1.259\ 580(5) \times 10^{-5}$
12	$1.019\ 187(5) \times 10^{-5}$	$0.759\ 620(5) \times 10^{-5}$
13	$0.679\ 575(5) \times 10^{-5}$	$0.469\ 973(5) \times 10^{-5}$
14	$0.410\ 825(5) \times 10^{-5}$	$0.296\ 641(5) \times 10^{-5}$
15	$0.252\ 108(5) \times 10^{-5}$	$0.189\ 309(5) \times 10^{-5}$
16	$0.155\ 786(5) \times 10^{-5}$	$0.121\ 749(5) \times 10^{-5}$
n	$\ell = n - 2, j = \ell + \frac{1}{2}$	$\ell = n - 1, j = \ell + \frac{1}{2}$
9	$28.939\ 225(5) \times 10^{-5}$	$14.918\ 400(5) \times 10^{-5}$
10	$16.589\ 245(5) \times 10^{-5}$	$9.141\ 150(5) \times 10^{-5}$
11	$10.111\ 871(5) \times 10^{-5}$	$5.882\ 197(5) \times 10^{-5}$
12	$6.331\ 080(5) \times 10^{-5}$	$3.940\ 256(5) \times 10^{-5}$
13	$4.318\ 998(5) \times 10^{-5}$	$2.729\ 475(5) \times 10^{-5}$
14	$2.979\ 937(5) \times 10^{-5}$	$1.945\ 279(5) \times 10^{-5}$
15	$2.116\ 050(5) \times 10^{-5}$	$1.420\ 631(5) \times 10^{-5}$
16	$1.540\ 181(5) \times 10^{-5}$	$1.059\ 674(5) \times 10^{-5}$

**Table 1.3** Calculated values for the coefficient  $G_{SE}(Z\alpha)$  with  $Z = 14, 16$  from [53]. The numbers in parentheses are standard uncertainties in the last figure.

n	Z	$\ell = n - 2, j = \ell - \frac{1}{2}$	$\ell = n - 1, j = \ell - \frac{1}{2}$
13	14	$0.676(9) \times 10^{-5}$	$0.469(9) \times 10^{-5}$
13	16	$0.682(4) \times 10^{-5}$	$0.468(7) \times 10^{-5}$
14	14	$0.403(8) \times 10^{-5}$	$0.296(9) \times 10^{-5}$
14	16	$0.408(6) \times 10^{-5}$	$0.296(9) \times 10^{-5}$
15	14	$0.243(9) \times 10^{-5}$	$0.184(7) \times 10^{-5}$
15	16	$0.249(3) \times 10^{-5}$	$0.191(9) \times 10^{-5}$
n	Z	$\ell = n - 2, j = \ell + \frac{1}{2}$	$\ell = n - 1, j = \ell + \frac{1}{2}$
13	14	$4.317(5) \times 10^{-5}$	$2.728(9) \times 10^{-5}$
13	16	$4.321(2) \times 10^{-5}$	$2.728(5) \times 10^{-5}$
14	14	$2.974(5) \times 10^{-5}$	$1.944(9) \times 10^{-5}$
14	16	$2.978(3) \times 10^{-5}$	$1.945(9) \times 10^{-5}$
15	14	$2.107(9) \times 10^{-5}$	$1.415(7) \times 10^{-5}$
15	16	$2.114(2) \times 10^{-5}$	$1.423(9) \times 10^{-5}$

certainty from the Planck constant since  $\nu = (E_{15} - E_{14})/h$ , and  $h$  drops out when calculating the frequency.

Table 1.5 gives sources and estimates of the various known uncertainties in the theory. By way of comparison, in hydrogen, the relative uncertainty from the two-photon term  $B_{60}$  for the 1S–2S transition is of the order of  $10^{-12}$  whereas in the

**Table 1.4** Transition frequencies between the highest- $j$  states with  $n = 14$  and  $n = 15$  in hydrogen-like helium and hydrogen-like neon.

Term	${}^4\text{He}^+$ $\nu$ (THz)	${}^{20}\text{Ne}^{9+}$ $\nu$ (THz)
$E_{\text{DM}}$	8.652 370 766 016(43)	216.335 625 5749(11)
$E_{\text{RR}}$	0.000 000 000 000	0.000 000 000 1
$E_{\text{QED}}$	-0.000 000 001 894	-0.000 001 184 1
Total	8.652 370 764 122(43)	216.335 624 3909(11)

$n = 14$  to  $n = 15$  Rydberg transitions the QED relative uncertainties are orders of magnitude smaller, as indicated in that table. The convergence of the expansion of the QED corrections in powers of  $Z\alpha$  is significantly faster for Rydberg transitions, because of the smallness of the higher-order terms for the high- $\ell$  states compared to S states.

**Table 1.5** Sources and estimated relative standard uncertainties in the theoretical value of the transition frequency between the highest- $j$  states with  $n = 14$  and  $n = 15$  in hydrogen-like helium and hydrogen-like neon.

Source	$\text{He}^+$	$\text{Ne}^{9+}$
Rydberg constant	$5.0 \times 10^{-12}$	$5.0 \times 10^{-12}$
Fine-structure constant	$3.3 \times 10^{-16}$	$8.2 \times 10^{-15}$
Electron-nucleus mass ratio	$5.5 \times 10^{-14}$	$1.1 \times 10^{-14}$
$a_e$	$5.1 \times 10^{-20}$	$1.3 \times 10^{-18}$
Theory: $E_{\text{RR}}$ higher order	$6.2 \times 10^{-17}$	$2.4 \times 10^{-14}$
Theory: $E_{\text{QED}} A_{81}$	$1.7 \times 10^{-18}$	$1.6 \times 10^{-14}$
Theory: $E_{\text{QED}} B_{60}$	$8.6 \times 10^{-18}$	$5.4 \times 10^{-15}$

### 1.5.4 Natural line widths

The advantages of using optical transitions between Rydberg states come with experimental trade-offs associated with a large spontaneous emission rate. Natural decay linewidths tend to be small for states from which electric dipole (E1) decay is forbidden (as in the case of the 2S level). In contrast, the spontaneous decay rate for a circular Rydberg state is dominated by an electric dipole E1 transition from the highest- $\ell$  value of the state  $n$  to the highest- $\ell$  value of the state  $n - 1$ .

Formally, the QED level shift given by Eq. (1.19) is the real part of the radiative correction. The complete radiative correction to the level can be written as  $\mathcal{E}_{\text{QED}} = E_{\text{QED}} - i\Gamma/2$  which is complex with an imaginary part proportional to the decay rate  $A = \Gamma/\hbar$  of the level. In the nonrelativistic framework, for a state with principal

quantum number  $n$  and angular momentum  $\ell = n - 1$ , the dominant decay mode is an E1 transition to state with  $n' = n - 1$  and  $\ell' = n' - 1$  [58]. Ref. [58] gives the corresponding expression for the decay rate, which is the nonrelativistic limit of the imaginary part of the level shift:

$$\Gamma_n \rightarrow hcR_\infty Z^4 \alpha^3 \frac{4n^{2n-4}(n-1)^{2n-2}}{3(n-\frac{1}{2})^{4n-1}}. \quad (1.21)$$

The imaginary part of the level shift gives the natural width of the level, and when this is taken into account, the resonant frequency of the transition between states with quantum numbers  $n$  and  $n - 1$ , as a function of the frequency of the applied laser field, has a full width at half maximum given by  $\Gamma_n + \Gamma_{n-1}$ . A measure of the quality of the line for making precision measurements is the ratio of the transition energy to the resonance width, given by

$$Q = \frac{E_n - E_{n-1}}{\Gamma_n + \Gamma_{n-1}} \rightarrow \frac{3n^2}{4\alpha(Z\alpha)^2} + \dots, \quad (1.22)$$

where the expression on the right is the asymptotic form as  $n \rightarrow \infty$  of the nonrelativistic value. Figure 1.6 gives a contour plot of the values of  $n$  and  $Z$  that give a specified value of  $Q$  based on Eq. (1.21).

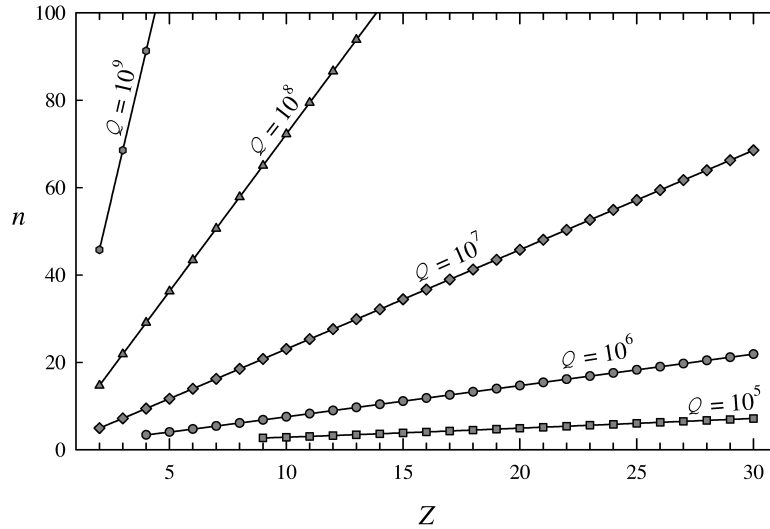


**Fig. 1.6** Graph showing combinations of nuclear charge  $Z$  and approximate  $n$  values that give the same ratio of the transition frequency to the natural linewidth of the transition resonance between circular states of one-electron ions with principal quantum number  $n$  and  $n - 1$ .

In addition to a width of the resonance, there can be an asymmetry in the line shape that affects the relationship between the measured frequency distribution and the level splitting. Such effects have been shown to be small by Low [59], of order  $\alpha(Z\alpha)^2 E_{\text{QED}}$ . For example, for the 1S–2S transition in hydrogen, they are completely negligible at the current level of experimental accuracy [60]. However, for Rydberg states of hydrogen-like ions, particularly at higher- $Z$ , asymmetries in the line shape could be more significant. Such effects, some of which might depend on the detailed configuration of the experiment, can be calculated if necessary [12].

## 1.6 Experiment

As discussed in Sec. 1.5, Rydberg states of hydrogenlike ions with  $\ell > 2$  essentially avoid a number of problems associated with either higher-order binding corrections to QED interactions or the nuclear size effect in Lamb shift predictions. In the cases considered for planned experiments, the higher-order QED corrections for Rydberg states are smaller by a factor of about  $10^7$  compared to S states while the nuclear size effect is completely negligible, providing significant advantages in making accurate predictions.

Of particular interest are Rydberg states with maximum angular momentum or *circular states*, so-called because the probability density is significant only in an annular region centered on the nucleus. In addition to aforementioned advantages, other useful features of circular states include: (1) the longest lifetime in a given shell  $n$ , and (2) suppressed Stark effect. In fact, circular Rydberg states of hydrogen in the microwave regime have been used in very precise measurements of transition frequencies [61]; as a result, a determination of the Rydberg constant has been made with a  $2.1 \times 10^{-11}$  relative uncertainty [61]. In Fig. 1.4 we compare this result based upon circular-state transitions with more recent determinations of the Rydberg constant. Unfortunately, the precision of the hydrogen circular-state measurements is not sufficient to help resolve the large discrepancy between the  $\mu\text{p}$  measurement and the hydrogen measurements (CODATA). In retrospect, the large dipole moments in circular Rydberg states of hydrogen would significantly increase the measurement uncertainty due to the possible perturbations from the dipole-dipole interaction between Rydberg atoms [62]. In contrast, such dipole-dipole interaction would be orders of magnitude smaller between one-electron Rydberg ions since the wavefunction is concentrated more tightly around a highly-charged nucleus.

Experiments with cold, one-electron Rydberg ions may be possible for a wide range of nuclear charge  $Z$  and angular momentum  $\ell$ . A considerable array of tools and techniques have emerged in the last two decades which enable “engineered atoms” to be formed in traps and tailored in specific states of experimental interest. Cooling techniques [63] routinely used with singly- or doubly-ionized atoms, for instance, can be exploited to cool highly-charged ions. Man-made quantum systems—for example, antihydrogen [64] or a single electron in a Penning trap [8]—have the potential to extend the range of precision measurements that probe nature. In this

section, we describe an experimental effort at NIST to produce one-electron ions in Rydberg states by isolating bare nuclei in a trap for recombination via electron capture from laser-excited alkali atoms.

### 1.6.1 Source of fully-stripped ions

Various methods have been used to produce Rydberg states [13]. Generally, one (or a combination) of the following mechanisms is used: (1) electron impact excitation, (2) photoexcitation, or (3) charge exchange. High angular-momentum states present some challenges when dealing with highly-charged ions. Electron impact excitation from the ground state tends to produce low- $\ell$  Rydberg states since it changes angular momentum by only one unit. Even for low- $Z$  one-electron ions, lasers with the proper frequency are not readily available for photoexcitation from the ground state. On the other hand, recombination by electron capture from a highly-excited atom produces Rydberg states with high- $\ell$ ; it is noteworthy that, following charge exchange, the recombined Rydberg ion tends to evolve via radiative cascade towards a circular state (maximum angular momentum) [67].

To use charge exchange for producing hydrogenlike ions, fully-stripped ions (bare nuclei) must be isolated in a trap. Fully-stripped ions can be obtained from an

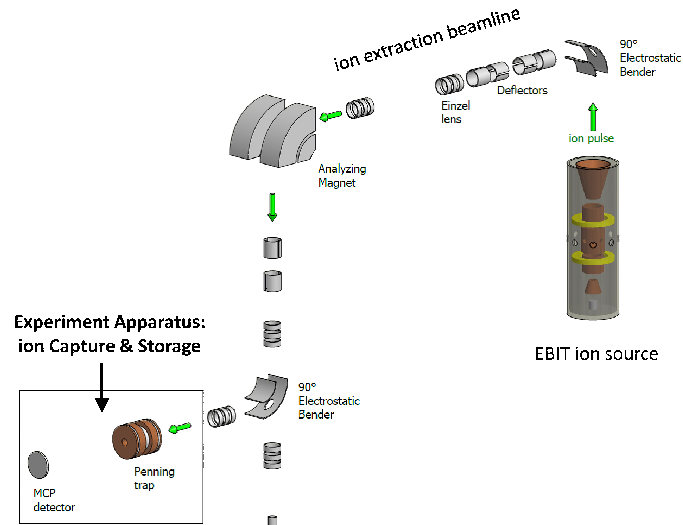


**Fig. 1.7** Simplified schematic of the experimental set-up (not to scale). Highly stripped ions are produced in an EBIT (right). Extracted ion pulses are transported to an analyzing magnet in the beamline. Detailed descriptions of the extraction beamline have been published in [65, 66]. Ions of a selected charge state are deflected by the analyzing magnet into the vertical beamline, where a 90-degree bender deflects them into the experimental apparatus (left).

electron beam ion trap (EBIT). An EBIT has been in operation at NIST since 1993 [68]. The EBIT at NIST has an existing beamline for ion extraction [66]. Figure 1.7 provides a simplified schematic diagram of the experimental set-up. As discussed in the next section, we recently demonstrated that a compact Penning trap [69] can be used for capturing ions extracted from the EBIT at NIST.

Highly-charged ions (HCI) are produced in an EBIT by repeated electron impact ionization of atoms injected as a neutral gas target via a nozzle (alternatively, low charge-state metal ions can be injected from a metal-vapor vacuum arc [MeVVA] source [70]). In an EBIT, a nearly-monoenergetic electron beam is accelerated through high voltage  $U_e$  to reach high energies  $eU_e$  as it travels through the axis of a stack of three electrodes called drift tubes; for the EBIT at NIST, an electron beam current as high as 150 mA can be used, accelerated to energies up to 30 keV. Coaxial with the drift tubes is a strong magnetic field ( $\approx 3$  T) which compresses the radial extent of the electron beam, yielding very high current density. Confinement of positively-charged ions is similar to that in a Penning trap, with the drift tubes biased to form an electrostatic potential well along the trap symmetry axis; however, radial confinement of ions is dominated by attraction to the tightly-compressed, axial electron beam. Confined ions collide with the intense electron beam repeatedly and are ionized to successively higher charge states limited by the kinetic energy of the electron beam.

A mixture of several charge states is produced in an EBIT, bounded by the ionizing energy of the electron beam, with a relative distribution determined by various tuning parameters. For the purpose of capturing and isolating the ions in an experimental apparatus, the HCI mixture is extracted in bunches by quickly ramping the EBIT middle drift tube up in voltage. The extracted ion pulse accelerates out of the drift tube region, with each ion of charge number  $Q$  acquiring substantial kinetic energy ( $\approx QeU_e$ ) as it departs from the potential “hill” that accelerates the electron beam. Typical ion pulse energies for the experiments of interest here are between 2000  $Q$  eV and 4000  $Q$  eV. The process of slowing and capturing the extracted ions in a compact Penning trap is discussed in detail in a forthcoming publication, and is briefly described below in Sec. 1.6.2.

During ion extraction, an ion pulse from the EBIT is injected vertically into the extraction beamline (described elsewhere [66]). As shown in Figure 1.7, a 90-degree electrostatic bender turns the ion pulse into the horizontal beamline, which transports the ion bunch to an analyzing magnet located  $\approx 3.8$  m from the EBIT. The analyzing magnet allows selection of one specific ion charge state by adjusting its magnetic field to the proper value necessary for deflecting an ion of a chosen mass/charge ratio into the vertical section of the beamline. Figure 1.8 illustrates the selection of a specific charge state by controlling the magnetic field of the analyzing magnet. Downstream in the vertical beamline, another 90-degree electrostatic bender is used to divert the ion pulse to the experimental apparatus as illustrated in Figure 1.9, where ions can be detected on a Faraday cup or a microchannel plate. The total path length from the EBIT to the compact Penning trap in the experimental apparatus is  $\approx 7.2$  meters.

### 1.6.2 Capturing bare nuclei in a compact Penning trap

We have recently demonstrated that a compact Penning trap can be useful for capturing ions extracted from an EBIT [69]. The experimental apparatus shown in Figure 1.9 was designed to utilize the remaining space ( $\approx 1\text{m}^3$ ) at the end of the ion extraction beamline. It incorporates a compact Penning trap for capturing ion pulses extracted from the EBIT. A Penning trap can be made very compact by embedding annular rare-earth (NdFeB) magnets within its electrode structure. The electrode structure uses electrical-iron to close the magnetic circuit. The unitary architecture of this two-magnet, compact Penning trap is represented in Figure 1.10, with a three-dimensional rendering shown in the inset of Figure 1.9; a more detailed description has been presented in Ref. [69]. The endcap electrodes have holes to allow passage of ions along the trap axis. Not shown in Fig. 1.9 are the vacuum pumps (non-evaporable getter, turbo-molecular and ion pumps) which evacuate the room-temperature chamber to a residual gas pressure of  $\approx 1.2 \times 10^{-7}$  Pascal (or  $9 \times 10^{-10}$  Torr).

An ion beam or pulse entering the apparatus is steered by two orthogonal pairs of deflection plates, and focussed by an Einzel lens into the compact Penning trap. The electrodes in the trapping region have been carefully designed to optimize ion capture. Details on capturing ions with a compact Penning trap are presented in a forthcoming publication [71]. Here we give a brief summary.

The axial confinement well of the compact Penning trap is formed by symmetrically biasing the endcaps to higher electrical potential than on the ring electrode,

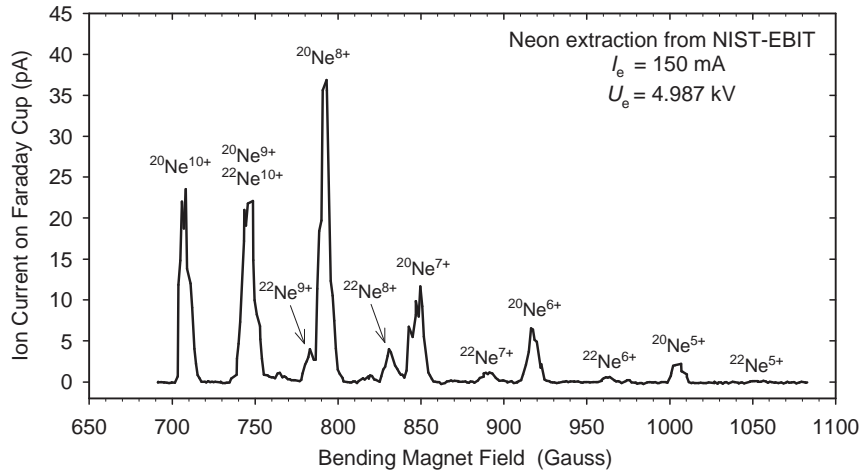


**Fig. 1.8** Charge states of neon resolved by the analyzing magnet, detected on a Faraday cup near the bottom of the vertical beamline. The Faraday cup signal is plotted as a function of the magnetic field generated by the analyzing magnet. The leftmost peak corresponds to fully-stripped  $^{20}\text{Ne}^{10+}$  (bare nuclei).

typically between 10V and 40V. In preparation for injecting an ion pulse into the Penning trap, the potential of the “front” endcap facing the incoming ion pulse is momentarily lowered below the ring electrode potential. The trap is kept open during the transit of the ions pulse from the EBIT to the compact Penning trap. Ions steered and focussed into the Penning trap are captured by switching the front endcap rapidly back to its high potential setting, ideally when the ions are turning around from the “back” endcap. Simulations aid the design of trap components to attain good capture efficiency. Various operating parameters are also important; foremost are: (1) proper timing for closing the trap; and (2) matching the electrical potential of the compact Penning trap to the extraction energy in order to slow the ions as much as possible in the trapping region. Various ion species extracted from

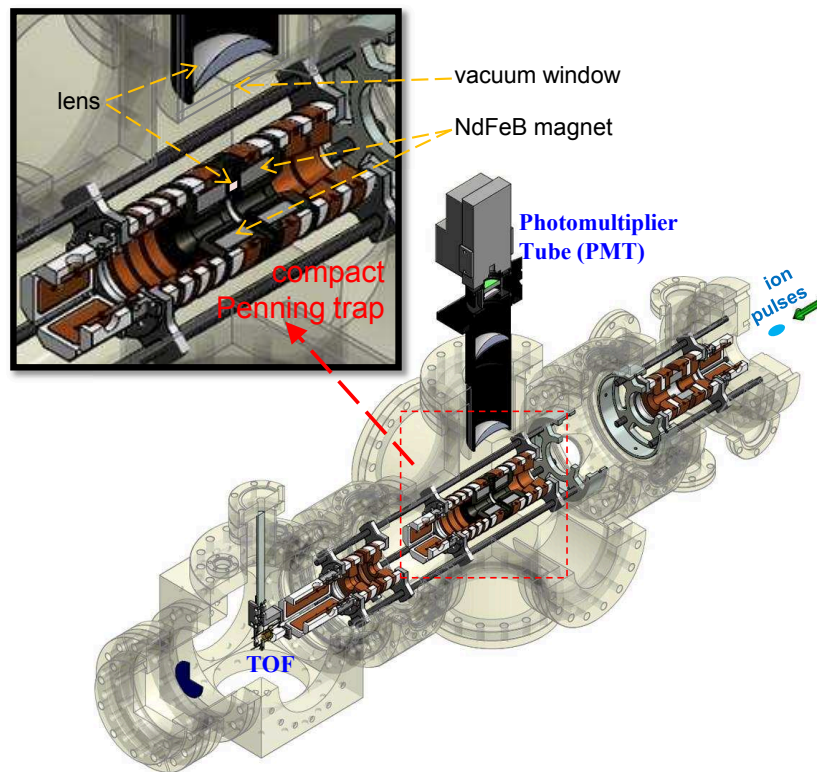


**Fig. 1.9** Experimental apparatus for capturing ions extracted from an EBIT using a compact Penning trap. Quarter-cut three-dimensional representation of major components with vacuum chamber in lighter shades. Inset shows a zoomed view of the unitary Penning trap and the light collection optics. Ions enter the apparatus from the right hand side.

an EBIT (including:  $\text{Ne}^{10+}$ ,  $\text{Ne}^{9+}$ ,  $\text{Ne}^{8+}$ ,  $\text{Ar}^{16+}$ ,  $\text{Ar}^{15+}$ ,  $\text{Ar}^{14+}$ ,  $\text{Ar}^{13+}$ , and  $\text{Kr}^{17+}$ ) have been captured and isolated in the two-magnet Penning trap [72].

The apparatus provides relatively easy access to the stored ions along several directions for various experiments. Occupying less than  $150 \text{ cm}^3$  of volume, the compact Penning trap is readily configured with several detectors. In particular, the ring electrode has four equidistant holes to provide midplane line-of-sight access to the stored ions. The trap is centered on a six-way cross with one of the ring electrode holes aligned with the vertical axis of the vacuum cross, and an orthogonal hole aligned with the horizontal window. As illustrated in the inset of Fig. 1.9, the top hole in the ring electrode has an embedded aspheric lens which, together with the lens system mounted outside the top window, collects and focusses light emitted by the trapped ions into a photomultiplier. Very recently, highly charged ions isolated in this unitary Penning trap have been used in experiments to observe forbidden radiative decay [73].

Stored ions can be detected also by ejection to a retractable, time-of-flight (TOF) micro-channel plate (MCP) detector, with  $\approx 1 \text{ ns}$  response time to resolve different charge states. Alternatively, if the TOF detector is retracted, a position-sensitive MCP detector can be used. Details of the ion detection scheme are in [69]. These capabilities have been useful in fine-tuning the ion beam and in measuring the storage lifetime of captured ions [72, 74].

Fully-stripped neon ions (bare  $\text{Ne}^{10+}$  nuclei) have been extracted from an EBIT and captured in the unitary Penning trap. An ion cloud in a Penning trap attains dynamical equilibrium by rotation (spin) about the trap axis to generate a  $\mathbf{v} \times \mathbf{B}$  compressive force which counter-balances the Coulomb repulsion (or space-charge

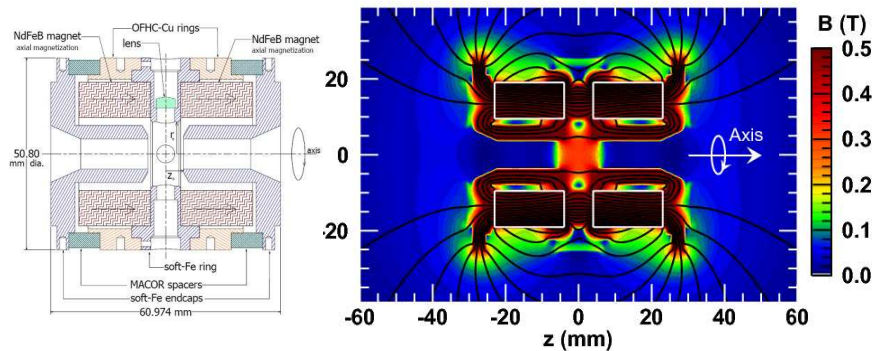


**Fig. 1.10** A Penning trap made extremely compact with a unitary architecture. (Left) Cross-sectional view showing 2 annular NdFeB magnets embedded within the electrode structure. Reentrant, soft-iron endcap electrodes are used to close the magnetic circuit to strengthen the field at the center. (Right) Calculated magnetic field generated by the two rare-earth magnets is represented in false color. More details are provided in [69].

repulsion) between ions. For most practical cases, an ion cloud expands radially if the rotation slows down due to some torque acting on the cloud (which may come from trap imperfections or misalignment). Radial expansion of the ion cloud can lead to number loss when some ions strike the wall of the ring electrode. Even in a well-constructed trap wherein cloud expansion is very slow, an ion can change charge state due to electron capture from residual gas atoms.

The charge-state composition of an ion cloud can be analyzed from the time-of-flight of ejected ions to the fast MCP detector. The endcap nearest the TOF detector is switched to 400 V below the ring voltage in about 50 ns, ramping out the ions in a pulse. Figure 1.11(a) shows the TOF signal of bare  $\text{Ne}^{10+}$  nuclei ejected to the detector after 1 ms of confinement in the two-magnet Penning trap. If there are multiple charge states, several peaks will be observed. Lower charge stages have later arrival times due to their smaller charge-to-mass ratio. Figure 1.11(b) illustrates the mixture of charge states produced from the charge exchange between a cloud of bare nuclei (initial state) and the background gas atoms, detected after 2 s confinement. The TOF is sufficiently fast to fully resolve the lower charge states produced

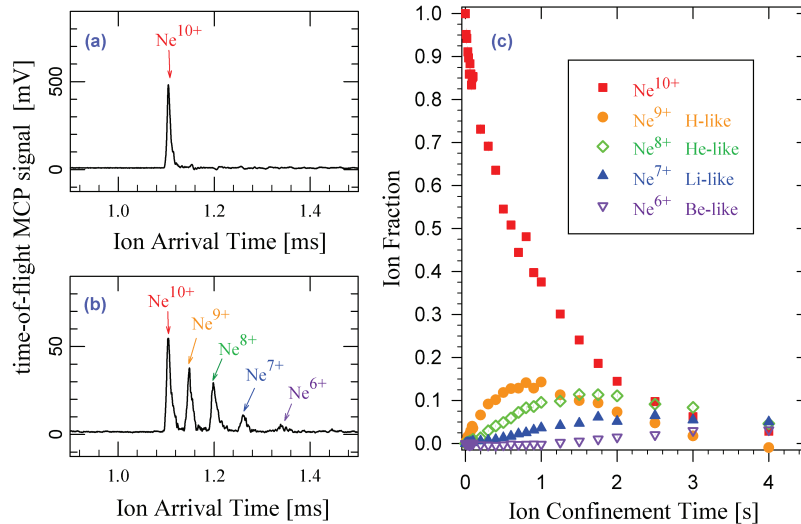


**Fig. 1.11** Time-of-flight detection of highly-charged ions ejected from the two-magnet Penning trap after various storage times [72, 69], showing charge-state evolution of captured bare nuclei due to electron capture from residual background gas. Neon ions are stored in the Penning trap for times ranging from 1 ms to 4 s, with applied potential difference  $\Delta V = 10$  V between the ring and endcap electrodes. In particular, output of the TOF detector is plotted versus arrival time (relative to the ejection trigger) for storage times of (a) 1 ms and (b) 2 s. The detector signal scale is magnified by a factor of 10 from (a) to (b). The TOF signal peak for each charge state is converted to ion counts in order to show (c) the evolution of charge states due to charge exchange, normalized to the initial population of  $\text{Ne}^{10+}$  ions observed at the 1 ms storage time. Error bars represent  $1\sigma$  uncertainty.

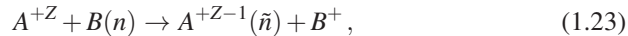
by charge exchange. Figure 1.11c shows the charge-state evolution as a function of confinement time.

Collisions with the residual gas atoms or molecules in the vacuum chamber deplete the initial ion species captured in the Penning trap. In Fig. 1.11c, the initial charge state ( $\text{Ne}^{10+}$  bare nuclei; red squares) decays exponentially with time constant 1.09(2) s, as lower charge states grow; the sum of all observed charge states decays with a longer time constant 2.41(6)s. The variation of these decay rates with the amount of residual gas is illustrated in Figure 1.12, showing their linear proportionality to the background gas pressure. Loss of stored bare nuclei is largely due to charge exchange. Ion cloud expansion can explain the decay of the charge-state sum [69]. It is noteworthy that the decay rates extrapolate to nearly zero, indicating that the compact Penning trap imperfections do not contribute significantly to the torque driving the ion cloud expansion. If the background gas pressure is reduced, for example by cooling the vacuum envelope with a cryocooler, then the lifetime of the charge state of interest can be lengthened (and the ion cloud expansion rate reduced) considerably.

### 1.6.3 Charge-exchange recombination: one-electron Rydberg ions

One-electron ions in high- $\ell$  Rydberg states have attractive features for testing theory. Undoubtedly challenging to realize, such elegantly-simple quantum system can be engineered using an array of tools and techniques that have emerged in atomic-molecular-optical physics within the last two decades. For example, production of cold antihydrogen at the European Laboratory for Particle Physics (CERN) demonstrated two ways for an antiproton to capture a positron in high- $\ell$  Rydberg states: (1) three-body recombination during positron cooling of antiprotons; or (2) positron capture from positronium in a two-stage charge-exchange mechanism [64]. In addition, Doppler-tuned laser spectroscopy of Rydberg states has been used to study the atomic cores of highly charged ions in crossed-beam experiments [75].

The effort underway at NIST will develop a unitary, compact Penning trap (Fig. 1.10) to facilitate the interaction of stored bare nuclei with an excited atomic beam for the formation of one-electron ions in Rydberg states via charge exchange. In the planned experiment, a beam of alkali atoms enters the compact Penning trap through one of the holes in the ring electrode and they are excited by lasers to Rydberg states. The charge-exchange reaction between a bare nucleus  $A$  of charge  $Z$  colliding a target atom  $B$  prepared in an excited state with a principal quantum number  $n$  is represented by the formula



where  $\tilde{n}$  is the principal quantum number of the one-electron ion  $A^{+Z-1}$  immediately after recombination. A classical-trajectory Monte Carlo (CTMC) method has been used to estimate the electron capture cross-section, with the low-velocity limit given

by [76]

$$\sigma_{cx} \approx 5.5Z\pi n^4 a_0^2, \quad (1.24)$$

which indicates that the large geometrical cross-section for a Rydberg target atom with radius  $r_n = n^2 a_0$  is further enhanced by a factor  $5.5Z$ .

CTMC simulations also showed that the excited electron in the target atom attempts to preserve its original orbital dimension and energy during the electron capture process, leading to an initial post-collisional quantum number distribution given by

$$n\sqrt{Z} \leq \tilde{n} \leq nZ, \quad (1.25)$$

with the most probable state being roughly  $\tilde{n} \approx [nZ + nZ^{1/2}]/2$  [76]. Results of crossed-beam experiments which studied ion-Rydberg atom collisions are consistent with this model [13, 77]. As an illustration, the CTMC model predicts that Ry-

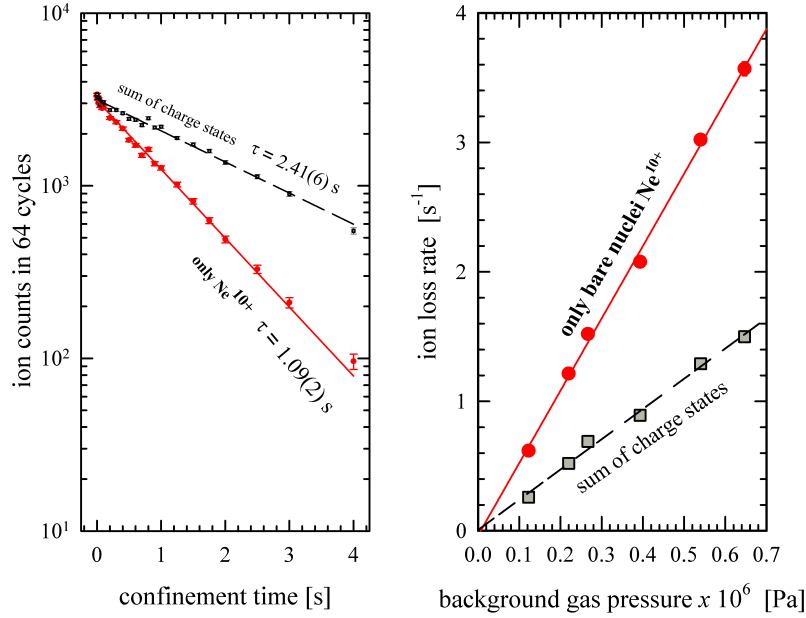


**Fig. 1.12** Loss rate of ions stored in the compact Penning trap. (Left) Exponential decay of detected ions as a function of confinement time. The vacuum chamber pressure for these measurements is  $\approx 1.7 \times 10^{-7}$  Pa ( $1.3 \times 10^{-9}$  Torr). (Right) The ion loss rate varies linearly with the residual gas pressure in the vacuum chamber. A voltage difference of  $\Delta V = 10$  V was applied between the ring and endcap electrodes of the Penning trap. Error bars represent  $1\sigma$  uncertainty. See Ref.[69] for more details.

rydberg states in the range  $63 < \tilde{n} < 200$  are obtainable for  $Ne^{10+}$  nucleus colliding with a target atom prepared in  $n = 20$  excited state, with the peak near  $\tilde{n} \approx 130$ .

## 1.7 Summary

With the assumption that the theory is correct, QED is used to determine values of the relevant fundamental constants by adjusting their values to give the best agreement with experiments [78]. The Rydberg constant, for example, is currently determined to  $5.0 \times 10^{-12}$  uncertainty by adjusting its value to give predictions of atomic transition frequencies that agree best with twenty-four spectroscopic measurements in hydrogen and deuterium. The accuracy of the Rydberg constant determination using hydrogen spectroscopy is limited by theoretical uncertainties associated with the nuclear-size effects and, to a lesser extent, the two-loop QED contributions. In such a comparison between theory and experiments, the proton radius can also be adjusted to give the best agreement.

Surprisingly, recent measurements of the Lamb shift in muonic hydrogen, when compared with QED calculations, require a proton radius that is almost seven standard deviations smaller than the radius inferred from hydrogen spectroscopy or electron scattering experiments. The discrepant proton-radius value obtained from muonic hydrogen Lamb shift measurements has a significant impact on the determination of the Rydberg constant if used together with spectroscopic measurements of hydrogen and deuterium. This has generated renewed interest in alternative measurements that are independent of the proton radius. Although transitions between circular states of neutral hydrogen have been measured in the microwave regime and yield such a value of the Rydberg constant, the uncertainty is larger than the aforementioned discrepancy, and may be dominated by large dipole-dipole interactions.

In view of the availability of optical frequency combs, earlier theoretical work at NIST has addressed the possibility of comparing theory with measurements of optical transitions between Rydberg states in one-electron ions isolated in a trap. Attractive features of using one-electron ions include the robustness of Rydberg states when the energy spacing between neighboring states is magnified by some power of a larger nuclear charge, making the Rydberg states more immune to external perturbations. Moreover, in contrast to neutral Rydberg atoms, the dipole-dipole interaction (which may have limited the MIT Rydberg hydrogen experiment [62]) would be orders of magnitude weaker due to the smaller orbitals around a stronger nuclear attraction. Finally, as reviewed here, recent calculations at NIST have shown that the theory of Rydberg states in one-electron ions is remarkably simplified for high angular momentum ( $\ell > 2$ ).

**Acknowledgements** Experimental work by S.M. Brewer and N.D. Guise has been supported by the Chemical Physics Program of the University of Maryland, and the Research Associateship Program of the U.S. National Research Council, respectively. Valuable contributions to the theory of Rydberg states have been made by U.D. Jentschura and B.J. Wundt.

## References

1. P.J. Mohr, B.N. Taylor, D.B. Newell, *Rev. Mod. Phys.* **84**(4), 1527 (2012)
2. G.W. Series (ed.), *The Spectrum of Atomic Hydrogen: Advances* (World Scientific, Singapore, 1988)
3. J.S. Rigden, *Hydrogen: the essential element* (Harvard University Press, Cambridge, Massachusetts, 2002)
4. P. Kusch, H.M. Foley, *Phys. Rev.* **72**, 1256 (1947)
5. W.E. Lamb, Jr., R.C. Retherford, *Phys. Rev.* **72**(3), 241 (1947)
6. W.E. Lamb, Jr., *Rep. Prog. Phys.* **14**, 19 (1951)
7. R.S. Van Dyck, Jr., P.B. Schwinberg, H.G. Dehmelt, *Phys. Rev. Lett.* **59**(1), 26 (1987)
8. L.S. Brown, G. Gabrielse, *Rev. Mod. Phys.* **58**(1), 233 (1986)
9. D. Hanneke, S. Fogwell, G. Gabrielse, *Phys. Rev. Lett.* **100**, 120801 (2008)
10. T. Hänsch, J. Alnis, P. Fendel, M. Fischer, C. Gohle, M. Herrmann, R. Holzwarth, N. Kolachevsky, T. Udem, M. Zimmermann, *Philos. Trans. R. Soc. London, Ser. A* **363**(1834), 2155 (2005)
11. F. Dyson. letter to G. Gabrielse, July 15 (2006)
12. U.D. Jentschura, P.J. Mohr, J.N. Tan, B.J. Wundt, *Phys. Rev. Lett.* **100**, 160404 (2008)
13. T.F. Gallagher, *Rydberg Atoms*, 1st edn. (Cambridge University Press, New York, 1994)
14. M. Fischer, N. Kolachevsky, M. Zimmermann, R. Holzwarth, T. Udem, T.W. Hänsch, M. Abgrall, J. Grünert, I. Maksimovic, S. Bize, H. Marion, F.P. Dos Santos, P. Lemonde, G. Santarelli, P. Laurent, A. Clairon, C. Salomon, M. Haas, U.D. Jentschura, C.H. Keitel, *Phys. Rev. Lett.* **92**, 230802 (2004)
15. M. Weitz, A. Huber, F. Schmidt-Kaler, D. Leibfried, W. Vassen, C. Zimmermann, K. Pachucki, T.W. Hänsch, L. Julien, F. Biraben, *Phys. Rev. A* **52**(4), 2664 (1995)
16. C.G. Parthey, A. Matveev, J. Alnis, R. Pohl, T. Udem, U.D. Jentschura, N. Kolachevsky, T.W. Hänsch, *Phys. Rev. Lett.* **104**, 233001 (2010)
17. C. Schwob, L. Jozefowski, B. de Beauvoir, L. Hilico, F. Nez, L. Julien, F. Biraben, O. Acef, A. Clairon, *Phys. Rev. Lett.* **82**(25), 4960 (1999)
18. O. Arnoult, F. Nez, L. Julien, F. Biraben, *Eur. Phys. J. D* **60**(2), 243 (2010)
19. S. Bourzeix, B. de Beauvoir, F. Nez, M.D. Plimmer, F. de Tomasi, L. Julien, F. Biraben, D.N. Stacey, *Phys. Rev. Lett.* **76**(3), 384 (1996)
20. D.J. Berkeland, E.A. Hinds, M.G. Boshier, *Phys. Rev. Lett.* **75**(13), 2470 (1995)
21. E.W. Hagley, F.M. Pipkin, *Phys. Rev. Lett.* **72**(8), 1172 (1994)
22. S.R. Lundeen, F.M. Pipkin, *Metrologia* **22**(1), 9 (1986)
23. G. Newton, D.A. Andrews, P.J. Unsworth, *Philos. Trans. R. Soc. London, Ser. A* **290**(1373), 373 (1979)
24. I. Sick, *Can. J. Phys.* **85**(5), 409 (2007)
25. J.C. Bernauer *et al.*, *Phys. Rev. Lett.* **105**, 242001 (2010)
26. I. Sick, in *Precision Physics of Simple Atoms and Molecules*, ed. by S.G. Karshenboim (Springer, Lect. Notes Phys. 745, Berlin, Heidelberg, 2008), pp. 57–77
27. Z. Zhan *et al.*, *Phys. Lett. B* **705**(1-2), 59 (2011)
28. G. Ron *et al.*, *Phys. Rev. C* **84**, 055204 (2011)
29. I. Sick, *Few-Body Syst.* **50**(1-4), 367 (2011)
30. I. Sick, *Prog. Part. Nucl. Phys.* **67**(2), 473 (2012)
31. C. Adamuscin, S. Dubnicka, A.Z. Dubnickova, *Prog. Part. Nucl. Phys.* **67**(2), 479 (2012)
32. R. Pohl, R. Gilman, G.A. Miller, K. Pachucki, (2013). ArXiv:1301.0905
33. R. Pohl *et al.*, *Nature* **466**(7303), 213 (2010)
34. R. Pohl *et al.*, *J. Phys. Conf. Ser.* **264**, 012008 (2011)
35. A. Antognini *et al.*, *Science* **339**(6118), 417 (2013)
36. A. Antognini, F. Kottmann, F. Biraben, P. Indelicato, F. Nez, R. Pohl, *Ann. Phys. (N.Y.)* **331**, 127 (2013)
37. P. Indelicato, *Phys. Rev. A* **87**, 022501 (2013)
38. E. Borie, *Ann. Phys. (N.Y.)* **327**(3), 733 (2012). ArXiv:1103.1772-v6

39. S.G. Karshenboim, V.G. Ivanov, E.Y. Korzinin, *Phys. Rev. A* **85**, 032509 (2012)
40. U.D. Jentschura, *Ann. Phys. (N.Y.)* **326**(2), 500 (2011)
41. U.D. Jentschura, *Ann. Phys. (N.Y.)* **326**(2), 516 (2011)
42. J.D. Carroll, A.W. Thomas, J. Rafelski, G.A. Miller, *Phys. Rev. A* **84**, 012506 (2011)
43. I. Sick, *Phys. Lett. B* **576**(1-2), 62 (2003)
44. J.C. De Vries, A precision millimeter-wave measurement of the rydberg frequency. Ph.D. thesis, MIT (2001)
45. T.W. Hänsch, *Rev. Mod. Phys.* **78**(4), 1297 (2006)
46. M. Hori, A. Dax, J. Eades, K. Gomikawa, R. Hayano, N. Ono, W. Pirkel, E. Widmann, H.A. Torii, B. Juhász, D. Barna, D. Horváth, *Phys. Rev. Lett.* **96**, 243401 (2006)
47. L.S. Ma, Z. Bi, A. Bartels, L. Robertsson, M. Zucco, R.S. Windeler, G. Wilpers, C. Oates, L. Hollberg, S.A. Diddams, *Science* **303**(5665), 1843 (2004)
48. A. Marian, M.C. Stowe, J.R. Lawall, D. Felinto, J. Ye, *Science* **306**(5704), 2063 (2004)
49. J.R. Sapirstein, D.R. Yennie, in *Quantum Electrodynamics*, ed. by T. Kinoshita (World Scientific, Singapore, 1990), chap. 12, pp. 560–672
50. M.I. Eides, H. Grotch, V.A. Shelyuto, *Phys. Rep.* **342**(2-3), 63 (2001)
51. G. Gabrielse, P. Larochele, D. Le Sage, B. Levitt, W.S. Kolthammer, R. McConnell, P. Richerme, J. Wrubel, A. Speck, M.C. George, D. Grzonka, W. Oelert, T. Seifzick, Z. Zhang, A. Carew, D. Comeau, E.A. Hessels, C.H. Storry, M. Weel, J. Walz, *Phys. Rev. Lett.* **100**, 113001 (2008)
52. U.D. Jentschura, P.J. Mohr, J.N. Tan, B.J. Wundt, *Can. J. Phys.* **87**(7), 757 (2009)
53. U.D. Jentschura, P.J. Mohr, J.N. Tan, *J. Phys. B* **43**, 074002 (2010)
54. E.H. Wichmann, N.M. Kroll, *Phys. Rev.* **101**(2), 843 (1956)
55. U.D. Jentschura, *Phys. Rev. A* **74**, 062517 (2006)
56. E.O. Le Bigot, U.D. Jentschura, P.J. Mohr, P. Indelicato, G. Soff, *Phys. Rev. A* **68**, 042101 (2003)
57. G. Audi, A.H. Wapstra, C. Thibault, *Nucl. Phys. A* **729**(1), 337 (2003)
58. H.A. Bethe, E.E. Salpeter, *Quantum Mechanics of One- and Two-electron Atoms* (Academic Press, New York, 1957)
59. F. Low, *Phys. Rev.* **88**(1), 53 (1952)
60. U.D. Jentschura, P.J. Mohr, *Can. J. Phys.* **80**(6), 633 (2002)
61. J.C. De Vries, A precision millimeter-wave measurement of the rydberg frequency. Ph.D. thesis, MIT (2001)
62. D. Kleppner. private communication (2012)
63. W.M. Itano, *et al.*, *Phys. Scripta* **T59**, 106 (1995)
64. G. Gabrielse, in *Advances in Atomic Molecular, and Optical Physics*, vol. 50, ed. by B. Bederson, H. Walthers (Elsevier, San Diego, 2005), pp. 155–217
65. L.P. Ratliff, E.W. Bell, D.C. Parks, A.I. Pikin, J.D. Gillaspay, *Rev. Sci. Instrum.* **68**, 1998 (1997)
66. L. Ratliff, J. Roberts, in *Trapping Highly Charged Ions: Fundamentals & Applications*, ed. by J. Gillaspay (Nova Science Publishers, Hauppauge, 2001), p. 257
67. M.R. Flannery, D. Vrinceanu, *Phys. Rev. A* **68**, 030502(R) (2003)
68. J.D. Gillaspay, L.P. Ratliff, J.R. Roberts, E. Takács, Highly charged ions: Publications of the ebit project, 1993-2001. Special Publication 972, NIST (2001)
69. J.N. Tan, S.M. Brewer, N.D. Guise, *Rev. Sci. Instrum.* **83**(2), 023103 (2012). DOI 10.1063/1.3685246. URL <http://link.aip.org/link/?RSI/83/023103/1>
70. G.E. Holland, C.N. Boyer, J.F. Seely, J.N. Tan, J.M. Pomeroy, J.D. Gillaspay, *Rev. Sci. Instrum.* **76**(7), 073304 (2005)
71. S.M. Brewer, N.D. Guise, J.N. Tan. Capture and isolation of highly charged ions in a compact penning trap. arXiv. Submitted to *Phys. Rev. A*
72. N.D. Guise, S.M. Brewer, J.N. Tan, ArXiv e-prints (2012)
73. S.M. Brewer, N.D. Guise, J.N. Tan. Observing forbidden radiative decay of highly charged ions in a compact penning trap. BAPS.2012.DAMOP.U3.8 (2012)
74. N.D. Guise, S.M. Brewer, J.N. Tan. Charge exchange and spectroscopy with isolated highly-charged ions. BAPS.2012.DAMOP.U3.6 (2012)

75. S.R. Lundeen, C.W. Fehrenbach, *Phys. Rev. A* **75**(3), 032523 (2007). DOI 10.1103/PhysRevA.75.032523
76. R. Olson, *J. Phys. B: Atom. Molec. Phys.* **13**, 483 (1980)
77. B.D. DePaola, M.T. Huang, S. Winecki, M.P. Stockli, Y. Kanai, S.R. Lundeen, C.W. Fehrenbach, S.A. Arko, *Phys. Rev. A* **52**, 2136 (1995)
78. P.J. Mohr, B.N. Taylor, *Rev. Mod. Phys.* **77**(1), 1 (2005)